Matter

CellPress

Article

High Volumetric Energy and Power Density Li_2TiSiO_5 Battery Anodes via Graphene Functionalization

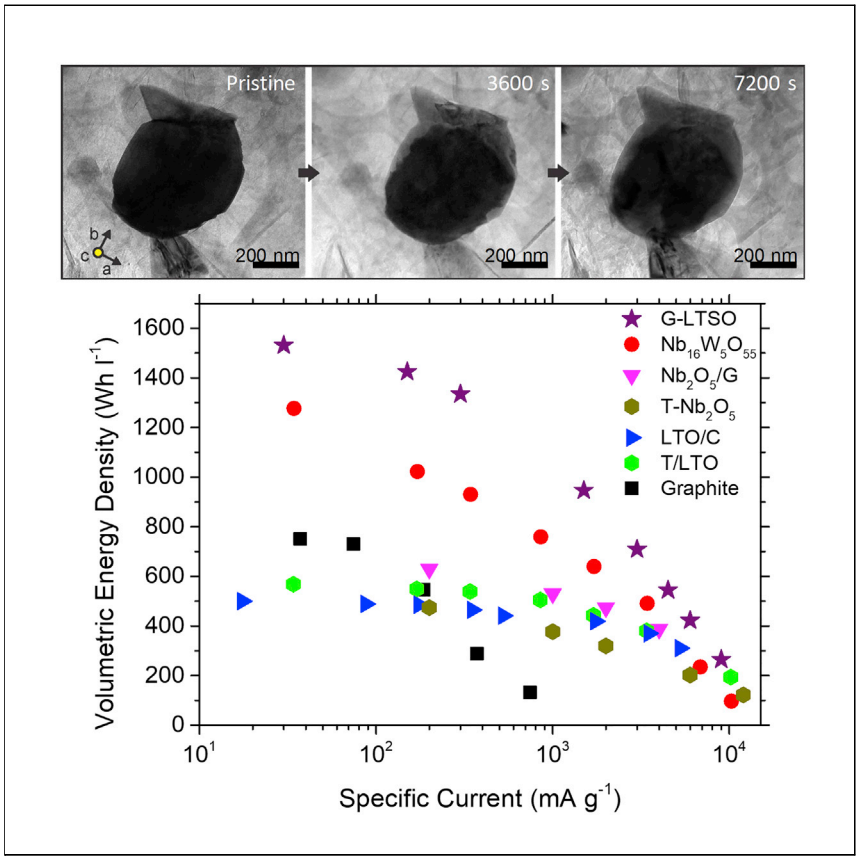

As a Li-ion battery anode, Li_2TiSiO_5 nanoparticles are conformally coated with graphene using a scalable ethyl cellulose-based solution process, which enables low overpotential and charge-transfer resistance, resulting in high rate performance with minimal risk for Li dendrite growth. Furthermore, the ethyl cellulose-based solution processing enables dense electrode packing and thus exceptionally high volumetric energy densities. With these advantages, graphene-functionalized Li_2TiSiO_5 shows significant potential as a next-generation Li-ion battery anode for high volumetric energy and power density applications.

Demonstrate
Proof-of-concept of performance with intended application/response

Jin-Myoung Lim, Sungkyu Kim, Norman S. Luu, ..., Vinayak P. Dravid, Kai He, Mark C. Hersam

m-hersam@northwestern.edu

HIGHLIGHTS

Li_2TiSiO_5 nanoparticles are coated with graphene using a scalable solution process

Graphene coating enables high rate capability with minimal risk for Li dendrites

Dense electrode packing results in exceptionally high volumetric energy density

Lim et al., Matter 3, 522–533
August 5, 2020 © 2020 Elsevier Inc.
https://doi.org/10.1016/j.matt.2020.07.017

CellPress

Matter

Article

High Volumetric Energy and Power Density Li_2TiSiO_5 Battery Anodes via Graphene Functionalization

Jin-Myoung Lim,[1,7] Sungkyu Kim,[1,2,3,7] Norman S. Luu,[1] Julia R. Downing,[1] Mark T.Z. Tan,[1] Kyu-Young Park,[1] Jacob C. Hechter,[1] Vinayak P. Dravid,[1,2] Kai He,[1,2,4] and Mark C. Hersam[1,5,6,8,*]

SUMMARY

The realization of lithium-ion battery (LIB) anodes with high volumetric energy densities and minimal Li plating at high rates remains a key challenge for emerging technologies, including electric vehicles and grid-level energy storage. Here, we present graphene-functionalized Li_2TiSiO_5 (G-LTSO) as a high volumetric energy and power density anode for LIBs. G-LTSO forms a dense electrode structure with electronically and ionically conductive networks that deliver superior electrochemical performance. Upon lithiation, *in situ* transmission electron microscopy reveals that graphene functionalization yields minimal structural changes compared with pristine LTSO, resulting in high cycling stability. Furthermore, G-LTSO exhibits not only high charge and discharge capacities but also low overpotentials at high rates with minimal voltage fading due to reduced formation of a solid-electrolyte interphase. The combination of highly compacted electrode morphology, stable high-rate electrochemistry, and low operating potential enables G-LTSO to achieve exceptional volumetric energy and power densities that overcome incumbent challenges for LIBs.

INTRODUCTION

Lithium-ion batteries (LIBs) have been the most prevalent technology in the rechargeable battery market for the past two decades, with widespread applications ranging from portable electronic devices to electric vehicles (EVs). To enable EVs of increased size and range in addition to larger-scale applications such as grid-level energy storage, LIB electrodes must accommodate increasingly high volumetric energy and power densities.[1–3] Recent work has identified promising candidates for high-power cathode materials that also possess significant improvements in energy density.[4] However, research on anode materials has not yet identified a clear and viable substitute for graphite, particularly for applications that require both high volumetric energy and power densities.[5,6]

Despite their widespread use in commercial LIBs, graphite anodes are vulnerable to localized overpotentials during fast charging at low operating potentials (<0.1 V versus Li/Li^+), which results in a high-impedance solid-electrolyte interphase (SEI) and plated Li metal. The resulting Li dendrite formation causes internal short circuits, which reduces the electrochemical performance and leads to major safety issues.[7–10] Although alloying anode materials such as Si promise remarkably large specific capacity (e.g., Si has a theoretical capacity of 4,200 mAh g^{-1} upon full lithiation to $Li_{22}Si_5$), severe volume expansion, material pulverization, and SEI formation hamper the use of alloying anode materials in practical applications.[11,12] In contrast, spinel

Progress and Potential

As electric vehicles increase in size and range, volumetric energy density and high rate capability have emerged as critical Li-ion battery performance metrics. While graphite has been the leader for Li-ion battery anodes for the past two decades, this material has severe limitations at high rates due to overpotentials that result in Li dendrite growth and significant safety issues. As an alternative to graphite, Li_2TiSiO_5 (LTSO) nanoparticles possess intrinsically high gravimetric energy densities and high rate capability with minimal risk for Li dendrite growth. However, pristine LTSO nanoparticles possess poor electrical conductivity and electrode packing density, which have prevented their full potential from being realized in Li-ion batteries. Here, LTSO nanoparticles are conformally coated with graphene using a scalable cellulose-based solution process, which enables low overpotential and dense electrode packing, resulting in exceptional volumetric energy densities at high rates.

lithium titanate ($Li_4Ti_5O_{12}$) is an anode material with improved safety and stability as a result of its "zero-strain" characteristic, but its high operating potential (>1.5 V versus Li/Li^+) and low theoretical capacity (175 mAh g^{-1}) substantially compromise energy density.[13–15] Recently, niobium oxide compounds have also been spotlighted as high-rate anode materials with large specific capacities of ~250 mAh g^{-1} and ~150 mAh g^{-1} at 0.2 C (34.3 mA g^{-1}) and 10 C (1.7 A g^{-1}), respectively.[16–18] However, similar to lithium titanate, niobium oxide compounds operate at high voltages (>1.0 V versus Li/Li^+), and consequently also possess modest energy densities. Although each of these anode materials has unique strengths that suggest viability in niche applications, a need still exists for a low-voltage anode material with minimal overpotential, stable cycling, and concurrently high volumetric energy and power density.

Toward this end, Li_2TiSiO_5 (LTSO) has emerged as a promising LIB anode material with a specific charge capacity of 350 mAh g^{-1} at 0.02 A g^{-1} and low operating potential of 0.28 V versus Li/Li^+. Nanoscale LTSO also has a high rate capability, exhibiting a specific capacity of 175 mAh g^{-1} at 1 A g^{-1},[19] in addition to minimal voltage fading when formed into composite electrodes with expanded graphite.[20] Moreover, LTSO nanoparticles have shown potential for Li-ion capacitor applications due to stable capacity-voltage curves with low polarization upon cycling.[21] However, nanoparticle-based electrodes formed via standard slurry coating methods have historically suffered from poor packing densities, which has implied relatively low volumetric energy densities.[22] While high pressure treatments can force nanoparticles into higher packing densities, the resulting electrodes suffer from low porosity, which blocks pathways for Li-ion diffusion, resulting in compromised high rate performance. Consequently, further innovation is required to preserve all of the desirable attributes of nanoscale LTSO, while also achieving high electrode packing and correspondingly high volumetric energy and power densities.

Here, we present a highly packed electrode design that achieves high volumetric energy and power density while maintaining the other advantages of nanoscale LTSO. This approach takes advantage of ethyl cellulose as a stabilizing polymer[23] to concurrently disperse LTSO nanoparticles and pristine graphene nanosheets in slurries that can be blade coated onto current collectors. Subsequent thermal processing pyrolyzes the ethyl cellulose, which compacts the electrodes, coats the LTSO with graphene (G-LTSO), and results in a continuous conductive carbon network throughout the electrode that facilitates charge transport and high rate performance. In addition, the conductive graphene coating mitigates SEI formation, reduces interfacial resistance, and minimizes overpotentials without compromising Li-ion diffusion, resulting in high volumetric energy and power densities. To gain atomic-scale insight into the graphene coating and the resulting electrochemical behavior of G-LTSO, *in situ* transmission electron microscopy (TEM) reveals that lithiation yields minimal structural changes and reduced amorphization for G-LTSO compared with pristine LTSO. The scalable nature of this solution-based electrode processing methodology suggests that G-LTSO can be seamlessly employed as a next-generation LIB anode for high volumetric energy and power density applications.

RESULTS AND DISCUSSION

Structural Analysis

The synthesis conditions for pristine LTSO and G-LTSO are provided in the Experimental Procedures section. As shown in Figure 1A, both as-synthesized LTSO and G-LTSO have a tetragonal structure in the *P4/nmm* space group, which agrees

[1]Department of Materials Science and Engineering, Northwestern University, 2220 Campus Drive, Evanston, IL 60208, USA

[2]NUANCE Center, Northwestern University, 2220 Campus Drive, Evanston, IL 60208, USA

[3]HMC, Department of Nanotechnology and Advanced Materials Engineering, Sejong University, 209 Neungdong-ro, Gwangjin-gu, Seoul 05006, Republic of Korea

[4]Department of Materials Science and Engineering, Clemson University, 515 Calhoun Drive, Clemson, SC 29634, USA

[5]Department of Chemistry, Northwestern University, 2220 Campus Drive, Evanston, IL 60208, USA

[6]Department of Electrical and Computer Engineering, Northwestern University, 2220 Campus Drive, Evanston, IL 60208, USA

[7]These authors contributed equally

[8]Lead Contact

*Correspondence: m-hersam@northwestern.edu

https://doi.org/10.1016/j.matt.2020.07.017

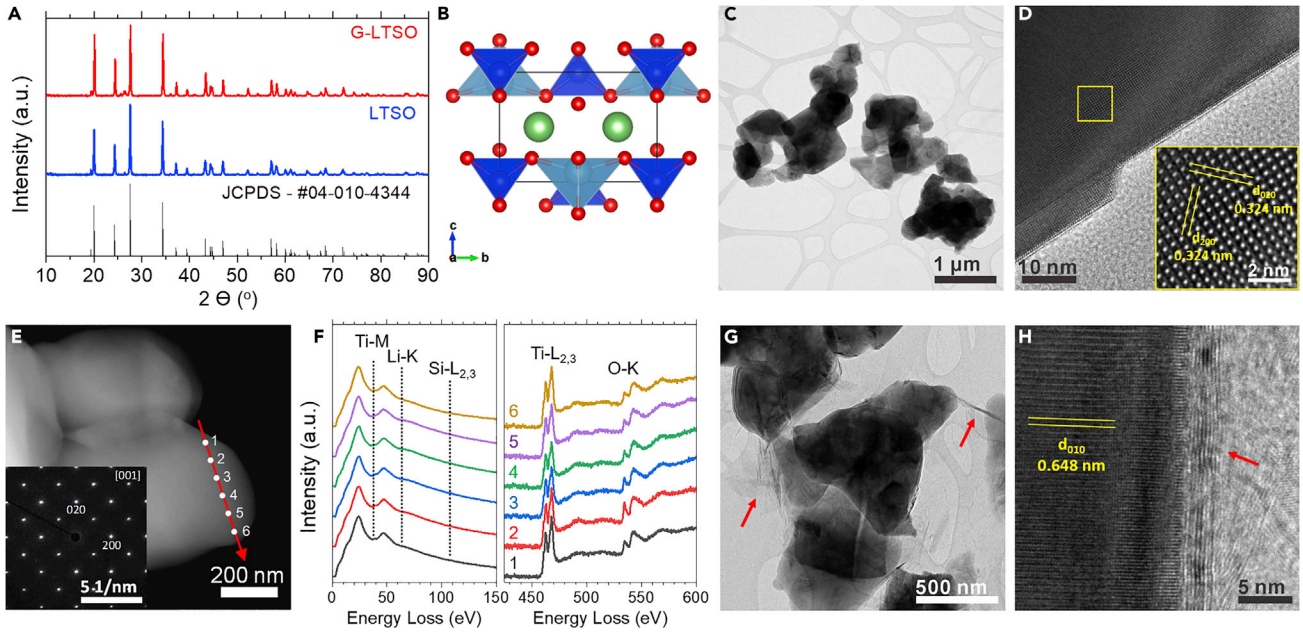

Figure 1. Structural Analysis of LTSO and G-LTSO

(A) XRD patterns of G-LTSO (red), LTSO (blue), and the reference (JCPDS #04-010-4344; black).

(B) Atomic model of the tetragonal LTSO structure with the P4/*nmm* space group: Ti (cyan), O (red), Si (blue), Li (green).

(C and D) (C) TEM and (D) HRTEM images of LTSO. The inset in (D) shows the pristine structure of [001]-oriented single-crystal LTSO.

(E and F) (E) HAADF-STEM image of an LTSO nanoparticle and (F) EELS profiles of Ti, Si, and O obtained along the red line in (E). The inset in (E) shows the SAED pattern of [001]-oriented single-crystal LTSO.

(G and H) (G) TEM and (H) HRTEM images of G-LTSO, with the red arrows indicating graphene nanoflakes.

well with the Joint Committee on Powder Diffraction Standards (JCPDS) database (#04-010-4344). As schematically depicted in Figure 1B, Ti ions (cyan) form octahedra with adjacent O ions (red), Si ions (blue) build tetrahedra with surrounding O ions, and Li ions (green) are located between the layers composed of TiO_6 octahedra and SiO_4 tetrahedra. The LTSO nanoparticles are approximately hundreds of nanometers in size as shown in the TEM and scanning electron microscopy (SEM) images in Figures 1C and S1A. The high-resolution TEM (HRTEM) images in Figure 1D confirm the tetragonal atomic arrangement of LTSO where the *a* lattice parameter is 0.648 nm, which is in close agreement with the JCPDS reference value (a = 0.644 nm). Figure 1E shows a high-angle annular dark-field scanning TEM (HAADF-STEM) image of a [001]-oriented pristine LTSO nanoparticle. Electron energy-loss spectroscopy (EELS) line profiles (Figure 1F) and energy-dispersive X-ray spectroscopy (EDS) mapping (Figure S2) confirm that the LTSO nanoparticles possess a uniform composition and electronic configuration. The TEM and SEM images in Figures 1G and S1B, respectively, show that G-LTSO particles have comparable sizes with the pristine LTSO particles and are coated and networked by graphene as indicated by the red arrows. The close-up HRTEM image in Figure 1H shows the detailed atomic structure of G-LTSO along the [010] orientation with the graphene layers again indicated by a red arrow. The *d*-spacing along the [010] orientation of G-LTSO is 0.648 nm, which is the same as the *d*-spacing of pristine LTSO.

In Situ Transmission Electron Microscopy Observation

Figure 2A sequentially shows *in situ* TEM images of the morphological changes in G-LTSO during lithiation. The electron beam was blanked to minimize irradiation

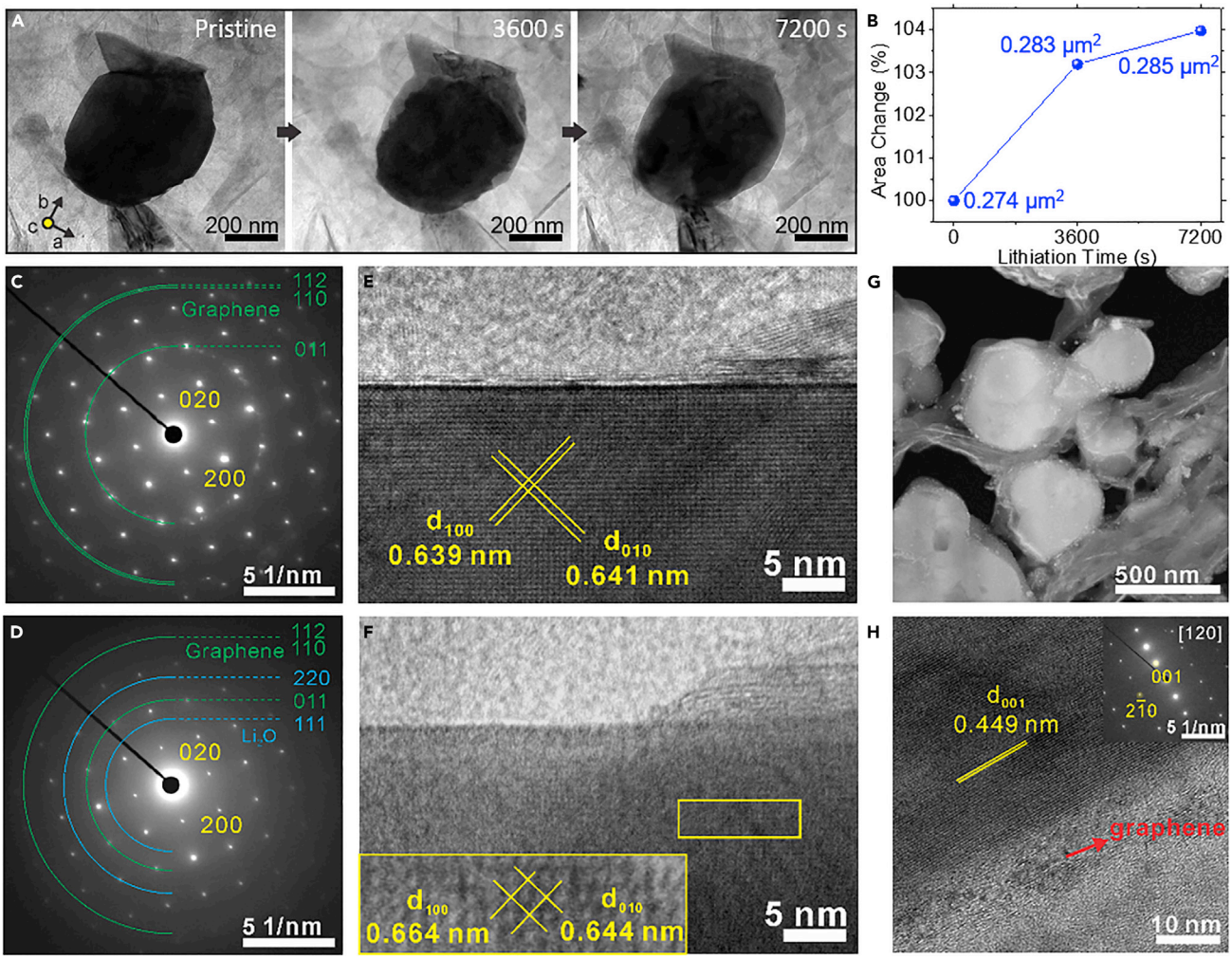

Figure 2. Transmission Electron Microscopy Analysis of Lithiated G-LTSO

(A and B) (A) Time-lapse TEM images of G-LTSO during the first lithiation step and (B) the area changes during lithiation.

(C–F) SAED patterns of G-LTSO (C) initially and (D) after lithiation, and the corresponding HRTEM images obtained from G-LTSO (E) before and (F) after lithiation.

(G and H) (G) STEM and (H) enlarged HRTEM images of a G-LTSO electrode sample prepared by focused ion beam milling after 300 cycles at 3 C.

effects except during image acquisition. After 7,200 s of lithiation, the original structure was well maintained except that the edge region started to show weak crystallinity caused by overlithiation.[19] To directly observe the effect of graphene encapsulation, *in situ* TEM was also performed on G-LTSO particles in a neighboring partially graphene-free region (Figure S3). Both the graphene-encapsulated and graphene-free regions were simultaneously connected to a lithium metal electrode, and the electron beam was blanked during *in situ* lithiation. As noted above, the LTSO structure is maintained in the graphene-encapsulated region (where the interlayer spacing of graphene increases due to the inserted Li ions), whereas the graphene-free region shows a perturbation to the lattice spacing of LTSO. In particular, we calculated the areal change of the G-LTSO nanoparticle during the *in situ* TEM measurement in Figure 2B, which shows a minimal 4% areal expansion from 0.274 μm^2 to 0.285 μm^2. In addition, following lithiation, the G-LTSO nanoparticle shows minimal changes in atomic structure as shown in Figures 2C–2F. *In situ* selected area electron diffraction (SAED) confirms that the graphene and LTSO diffraction patterns

of G-LTSO are well maintained during the lithiation process, which is further supported by the SAED radial profiles in Figure S4.

In order to investigate structural stability after cycling in fully assembled coin-cell electrodes, *ex situ* TEM was performed on a focused ion beam milled electrode sample after 300 cycles at a 3 C cycling rate. The LTSO particles encapsulated and networked by graphene remain intact in the G-LTSO electrode (Figure 2G), and the corresponding EDS maps indicate uniform distributions of Ti, Si, and O in the LTSO matrix and C in the graphene coating (Figure S5). In addition, the enlarged HRTEM image in Figure 2H indicates that the atomic structure of the LTSO matrix and the graphene coating is preserved following 300 cycles.

Electrochemical Characterization

The relative electrochemical performance of LTSO and G-LTSO coin-cell electrodes was evaluated by galvanostatic charge-discharge measurements at various C rates (1 C = 300 mA g^{-1}) in the potential window of 0.1–3.0 V versus Li/Li^+. Throughout this paper, the charge reaction denotes the insertion of Li into the anode, and the discharge reaction indicates the extraction of Li out of the anode. To compare the low rate behavior with and without graphene functionalization of LTSO, Figure S6A shows comparative charge-discharge profiles at a cycling rate of C/20. The G-LTSO electrode (dashed lines) shows more well-defined reaction plateaus at ~0.8 and ~0.28 V versus Li/Li^+ in comparison with the pristine LTSO electrode voltage profile, although the differential capacity (dQ/dV) analysis in Figure S6B reveals that both LTSO and G-LTSO have similar reaction potentials. In terms of lithiation capacity, G-LTSO charges to a specific capacity of 419.6 mAh g^{-1}, whereas pristine LTSO only charges to 302.4 mAh g^{-1} during the Li insertion process. G-LTSO also shows higher discharge capacity (242.3 mAh g^{-1}) compared with pristine LTSO (173.4 mAh g^{-1}) in the Li extraction process.

In addition to the capacity improvement at low rates, the graphene network contributes to the substantial increase of rate capability as shown in Figure 3A. Pristine LTSO shows poor rate capability due to its intrinsically low electrical conductivity.[19] In particular, the specific capacity of pristine LTSO dropped to ~75 mAh g^{-1} at 0.5 C and to ~35 mAh g^{-1} at 1 C as indicated in Figure S7A, and the dQ/dV analysis in Figure 3B reveals that distinct voltage plateaus were not observed at higher cycling rates beyond 0.1 C. On the other hand, G-LTSO shows a significantly improved high rate performance, including specific capacities exceeding 200 mAh g^{-1} at 1 C, 150 mAh g^{-1} at 5 C, 100 mAh g^{-1} at 15 C, and 50 mAh g^{-1} at 30 C, which restored back to ~225 mAh g^{-1} at 0.5 C as shown in Figures 3A and S7B. As demonstrated in Figure 3C, the G-LTSO dQ/dV profiles show well-defined voltage plateaus and relatively low overpotentials even at high cycling rates.

Cyclic retention tests at 1 C were also performed for both LTSO and G-LTSO after an activation cycle at C/20 as depicted in Figure 3D. As expected from the rate capability measurements, LTSO exhibits an initial specific capacity slightly below 50 mAh g^{-1} at 1 C, whereas the specific capacity of G-LTSO was initially ~200 mAh g^{-1}. Upon cycling, the specific capacity of G-LTSO gradually increased to 235 mAh g^{-1} at the 50th cycle, which indicates that the active material was gradually activated during cycling. This activation of G-LTSO partially recovers the capacity loss during the first activation cycle and results in a Coulombic efficiency slightly higher than 100%. In contrast, while LTSO also shows activation during cycling, its Coulombic efficiency is only ~93%, which implies that LTSO activates during charging but does not achieve full discharging. In other words, LTSO suffers from

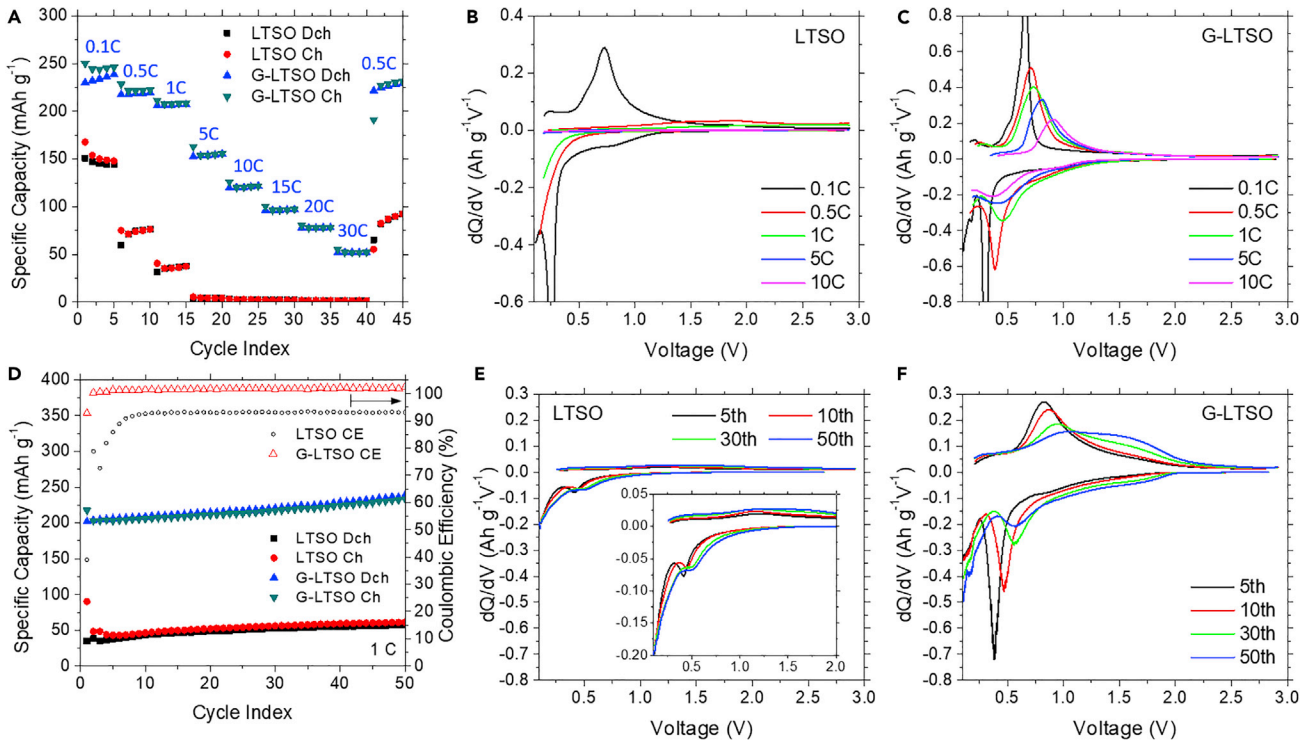

Figure 3. Electrochemical Measurements of LTSO and G-LTSO

(A) Rate capability at various C rates from C/10 to 30 C after an initial activation cycle at C/20.

(B and C) The corresponding dQ/dV profiles of (B) LTSO and (C) G-LTSO at 0.1 C, 0.5 C, 1 C, 5 C, and 10 C.

(D) Cycle performance and coulombic efficiency at 1 C after an initial activation cycle at C/20.

(E and F) The corresponding dQ/dV profiles of (E) LTSO and (F) G-LTSO at the 5th, 10th, 30th, and 50th cycles.

significant irreversibility between charging and discharging, whereas G-LTSO reversibly recovers a portion of the capacity lost in the first activation cycle. In terms of voltage fading, Figures 3E and 3F reveal that G-LTSO possesses significantly more stable voltage profiles than LTSO, whose voltage plateaus immediately disappear upon cycling.

Chemical and Electrochemical *Ex Situ* Characterization

To further investigate the origins of the improved electrochemical performance of G-LTSO, electrochemical impedance spectroscopy (EIS) analysis was performed before and after cycling. Figure 4A shows the impedance spectra at the open-circuit voltage (OCV) condition, where the fit is performed using the equivalent circuit model (ECM) depicted in Figure S8A. Figures 4B and 4C show the impedance spectra after the first charge and 20th charge, respectively, with the curves fit by the ECM depicted in Figure S8B. R_e denotes a high-frequency Ohmic resistance attributed to the electrolyte, R_{CT} represents the interfacial charge-transfer resistance, and W_{diff} represents Li-ion diffusion into the LTSO particles at lower frequencies. The constant phase elements (CPEs) describe the corresponding capacitances. Additional circuit elements are included for the impedance spectra in Figures 4B and 4C to model the resistance R_{SEI} and capacitance CPE_{SEI} resulting from the formation of the SEI upon cycling. The values of the resistances are displayed in Table S1. R_e for all cases show similar values in the range of 3.7–4.9 Ω, which is expected since the same electrolyte and the same cell configuration were used for all coin-cell measurements. At the OCV condition, both LTSO and

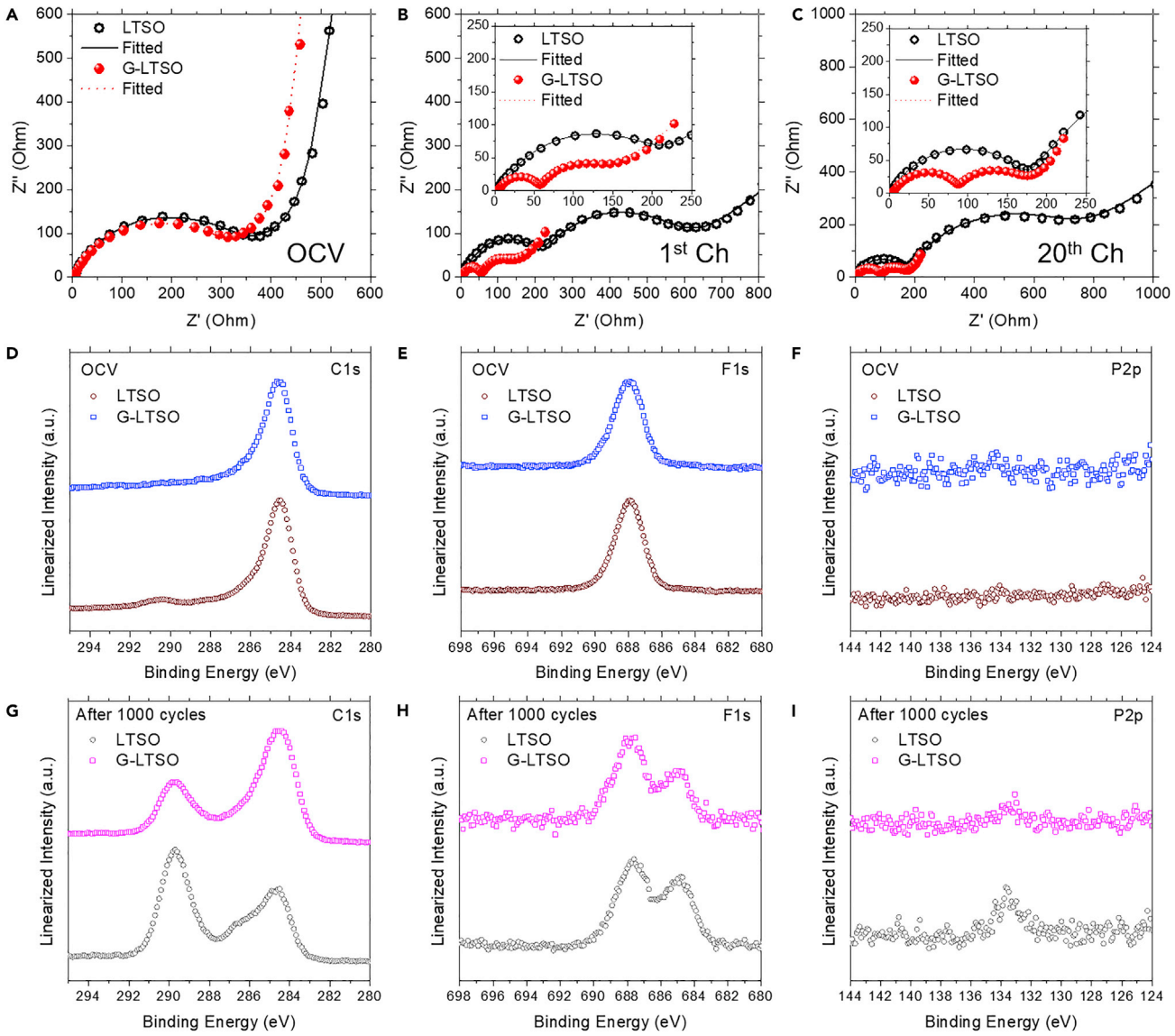

Figure 4. Electrochemical Impedance Spectroscopy and X-Ray Photoelectron Spectroscopy

(A–C) Electrochemical impedance spectra of LTSO (black) and G-LTSO (red) at (A) open-circuit voltage (OCV) condition, (B) after the 1st charge, and (C) after the 20th charge. The plotted circles are the measured spectra, and the lines are equivalent circuit model fits.

(D–I) (D) C1s, (E) F1s, and (F) P2p X-ray photoelectron spectra of LTSO (brown) and G-LTSO (blue) at OCV condition, and (G) C1s, (H) F1s, and (I) P2p X-ray photoelectron spectra of LTSO (gray) and G-LTSO (magenta) after 1,000 charge/discharge cycles.

G-LTSO impedance spectra show one semicircle that describes the charge-transfer resistance (R_{CT}), followed by the Warburg impedance (W_{diff}) at lower frequencies. Not only is the R_{CT} of G-LTSO (425.1 Ω) initially lower than that of LTSO (469.5 Ω) at the OCV condition but also the difference in R_{CT} between G-LTSO and LTSO increases during cycling. In addition, the R_{SEI} of LTSO after cycling is approximately a factor of 4 higher than G-LTSO. These extracted resistances confirm that graphene provides more efficient charge transport pathways in addition to minimizing the SEI layer for G-LTSO compared with pristine LTSO.

To probe chemical changes, LTSO and G-LTSO electrodes were characterized with X-ray photoelectron spectroscopy (XPS) following 1,000 charge/discharge cycles.

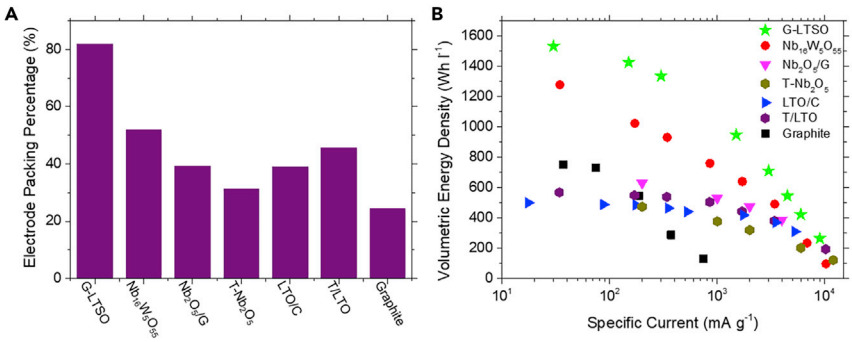

Figure 5. Electrode Packing Percentage and Volumetric Energy Density

(A) Electrode packing percentage of G-LTSO and other reported anode materials.

(B) Volumetric energy density as a function of specific current versus a 4 V cathode for G-LTSO and other reported non-alloying anode materials ($Nb_{16}W_5O_{55}$,[17] Nb_2O_5/G,[18] T-Nb_2O_5,[16] LTO/C,[25] T/LTO,[26] and graphite[27]).

Specifically, XPS spectra for C1s, F1s, and P2p before and after cycling provide insight into the formation of the SEI. Figures 4D and 4G show the C1s spectra at the OCV condition and after cycling, respectively. The major peaks in the C1s spectra are at ~284.6 eV and ~289.8 eV, which are assigned to graphitic C–C bonds and carbonate bonds, respectively, where the carbonate bonds can be attributed to Li_2CO_3 compounds formed in the SEI. As expected, Figure 4D shows that the carbonate peak is negligible before cycling for both LTSO and G-LTSO. However, after cycling, the carbonate peak is present in both materials but with a significantly higher intensity for LTSO in comparison with G-LTSO, which is consistent with suppressed SEI formation for G-LTSO as has been observed for other graphene-coated LIB electrodes.[24] For the F1s spectra, a prominent peak is evident at ~687.5 eV for LTSO and G-LTSO both before (Figure 4E) and after (Figure 4H) cycling due to the polyvinylidene fluoride (PVDF) that is used as the binder in all cases. However, after cycling (Figure 4H), the peak at ~684.5 eV is attributed to LiF in the SEI, which is again more pronounced for LTSO compared with G-LTSO. For the P2p spectra, the initial condition preceding cycling (Figure 4F) shows virtually no signal since the $LiPF_6$ salt was thoroughly rinsed from the electrodes using dimethyl carbonate. In contrast, after cycling (Figure 4I), P–O compounds from the SEI layer are evident at ~133.5 eV, with a higher signal for LTSO than for G-LTSO, which further corroborates SEI suppression by graphene in G-LTSO.

Benchmarking Battery Performance Metrics

As discussed above, graphene functionalization imparts several attributes to LTSO electrodes, including suppressed surface phase transformation and reduced SEI formation during electrochemical cycling. In addition, graphene imparts improved charge transport characteristics that minimize electrode impedance. As noted in the Introduction and the Experimental Procedures, the conformal graphene encapsulation is enabled by the ethyl cellulose polymer[23] that stabilizes the initial graphene/LTSO dispersion. The ethyl cellulose-based processing also promotes significant compaction of the electrode, resulting in an exceptional 80% electrode packing density (2.122 g cm^{-3}) compared with the theoretical electrode density (2.578 g cm^{-3}), which exceeds the electrode packing density of other reported state-of-the-art anode electrodes (e.g., $Nb_{16}W_5O_{55}$,[17] Nb_2O_5/G,[18] T-Nb_2O_5,[16] LTO/C,[25] T/LTO,[26] and graphite[27]) as shown in Figure 5A and Table S2. When this high electrode density is combined with the aforementioned low operating voltage,

G-LTSO enables exceptional volumetric energy density in comparison with other non-alloying anode materials. In addition, the high rate performance for G-LTSO implies that this record non-alloying anode volumetric energy density extends over a wide specific current range between 10^1 and 10^4 mA g^{-1}, as shown in Figure 5B and Table S3. Overall, these superlative battery performance metrics position G-LTSO as a leading candidate anode material for next-generation LIB technologies.

Conclusions

In conclusion, we have developed a high-performance LTSO anode through conformal graphene encapsulation. The graphene coating provides a high conductivity network in addition to suppressed SEI formation as confirmed by TEM and XPS, which minimizes impedance and results in improved electrochemical performance at high rates. *In situ* TEM further shows that G-LTSO undergoes reduced structural reorganization during electrochemical cycling, which underlies enhanced cycle lifetimes and reduced overpotentials. The ethyl cellulose polymer that is instrumental to the conformal graphene coating also enhances compaction of the electrode, which, in concert with the low operating voltage of G-LTSO, results in record-setting volumetric energy densities over a wide specific current range. The exceptional volumetric energy and power densities demonstrated here are likely to have broad impact on a diverse range of emerging LIB applications such as EVs and grid-level energy storage.

EXPERIMENTAL PROCEDURES

Resource Availability

Lead Contact

Further information should be directed to and will be fulfilled by the Lead Contact, Mark C. Hersam (m-hersam@northwestern.edu).

Materials Availability

This study did not generate new unique reagents.

Data and Code Availability

This study did not generate datasets and code.

Material Preparation

LTSO was synthesized following a previously published procedure.[19] Briefly, stoichiometric amounts of lithium hydroxide monohydrate (Sigma-Aldrich) dissolved in deionized water were mixed with stoichiometric amounts of titanium(IV) butoxide (Sigma-Aldrich) and tetraethyl orthosilicate (Sigma-Aldrich) dissolved in ethanol. After stirring for 3 h at room temperature, the mixed solution was dried at 80°C on a magnetic hotplate with continuous stirring. Subsequently, the dried powder was sintered at 870°C for 8 h under an argon atmosphere. Ethyl cellulose-stabilized graphene nanoflakes (Gr/EC) were prepared by following previously established methods[28] with the following modifications. In particular, a 10 mg/mL solution of ethyl cellulose (4 cP; Sigma-Aldrich) in 200-proof ethanol was mixed with graphite (+150 mesh; Sigma-Aldrich) with a ratio of graphite powder to ethyl cellulose solution of 100 g:1 L. Next, this mixture was shear mixed at 10,230 rpm for 2.5 h in a Silverson L5M-A high shear mixer and centrifuged at 6,500 rpm for 0.5 h using a Beckman Coulter J26 XPI centrifuge with a JLA 8.100 rotor. The supernatant was flocculated by mixing with 0.04 g/mL NaCl aqueous solution in a 9:16 weight ratio (NaCl(aq):supernatant), and then again centrifuged at 7,000 rpm for 6 min. The obtained solid was washed in deionized water, filtered, and dried to collect the Gr/EC powder with ~45 wt % graphene (Figure S9). The average size of the resulting

graphene nanoflakes was 140 nm in lateral width and 4.6 nm in thickness, and the morphology of the Gr/EC powder exhibits thin nanoflakes as shown in Figures S10 and S11, respectively. For graphene functionalization, Gr/EC dispersion was prepared by dissolving 0.111 g of Gr/EC powder in 15 mL of ethyl lactate/ethanol in a 1:2 volume ratio. The prepared dispersion was sonicated using a Fisher Scientific Model 500 Sonic Dismembrator with 3.175-mm (0.125-inch) tip at 30 W for 1 h. Subsequently, 0.95 g of as-synthesized LTSO was mixed in the sonicated dispersion and stirred for 1 h. The mixed dispersion was then bath sonicated for 1 h to ensure homogeneous dispersion of LTSO and graphene. This dispersion was cast onto Al foil and dried in a convection oven at 90°C, after which further calcination was performed at 250°C for 1 h in air. The final G-LTSO product was prepared by scraping the dried powder from the Al foil.

Characterization Details

The crystal structures of the as-prepared powders were characterized using X-ray diffraction (XRD) measured with a Scintag XDS2000 XRD system equipped with Cu-Kα radiation (λ = 1.5406 Å) with a 2θ range of 10°–90°. Particle morphologies and sizes were examined by SEM (Hitachi SU8030). Further structural characterization was performed using TEM (JEOL ARM 300CF and JEOL ARM 200CF). The TEM samples were prepared by a direct application of the pristine powder on a lacey carbon-supported TEM grid. For *in situ* TEM characterization, G-LTSO nanoparticles were mounted on TEM grids and connected to a Nanofactory TEM-STM holder, resulting in a half-cell inside the TEM. Li metal with a Li_2O solid electrolyte was connected to a piezo-driven metal probe in an Ar-filled glovebox and assembled with a TEM holder. During the *in situ* electrochemical reaction inside the TEM, a constant potential was maintained between the sample and Li metal. The *in situ* lithiation of G-LTSO was performed on a JEOL ARM 300CF TEM operated at 300 kV, and TEM images were recorded using a Gatan OneView-IS camera with 4,000 × 4,000 resolution. Focused ion beam milling was performed using an FEI Helios NanoLab DualBeam system, and XPS measurements were conducted using a Thermo Scientific ESCALAB 250Xi.

Electrochemical Measurements

Battery electrodes were prepared by fabricating an anode slurry with the active material, Super-P as a conducting agent, and PVDF as a binder dispersed in N-methyl-2-pyrrolidone with ratios of 60:30:10 for LTSO and 80:10:10 for G-LTSO. The well-mixed slurries were coated on Cu foils and dried at 80°C for 3 h, followed by further drying under vacuum overnight. CR2032 coin-type half-cells were assembled in an Ar-filled glove box by using glass fiber (Whatman) as a separator and Li metal as a counter electrode. 1.0 M $LiPF_6$ in ethylene carbonate/dimethyl carbonate with a 50:50 volume ratio was utilized as the electrolyte (Sigma-Aldrich). The loading levels of LTSO and G-LTSO were ~1.3 and ~1.5 mg cm^{-2}, and the electrode densities of each electrode were ~1.1 and ~2.1 g cm^{-3}, respectively. Galvanostatic charge and discharge tests were performed using an Arbin battery tester (LBT-20084) in the voltage range from 0.1 to 3.0 V versus Li/Li^+ after one-cycle activation at C/20 (15 mA g^{-1}). EIS was conducted using a Biologic VSP potentiostat.

SUPPLEMENTAL INFORMATION

Supplemental Information can be found online at https://doi.org/10.1016/j.matt.2020.07.017.

ACKNOWLEDGMENTS

This work was primarily supported by the Center for Electrochemical Energy Science, an Energy Frontier Research Center funded by the U.S. Department of Energy (DOE), Office of Science, Basic Energy Sciences (DOE award number DEAC02-06CH1157). Graphene powder production was supported by the National Science Foundation (NSF) Scalable Nanomanufacturing Program (NSF award number CMMI-1727846). This work made use of the Northwestern University NUANCE Center, which has received support from the Soft and Hybrid Nanotechnology Experimental (SHyNE) Resource (NSF award number ECCS-1542205), the Northwestern University Materials Research Science and Engineering Center (NSF award number DMR-1720139), and the State of Illinois. This research was also supported by the Basic Science Research Program through the National Research Foundation of Korea (NRF) funded by the Ministry of Education (NRF award number NRF-2020R1A6A1A03043435).

AUTHOR CONTRIBUTIONS

J.-M.L., S.K., and M.C.H. conceived the project. V.P.D., K.H., and M.C.H. supervised the project. J.-M.L., M.T.Z.T., and J.C.H. synthesized and fabricated the LTSO materials. J.R.D. produced the graphene nanoflakes. N.S.L. and J.-M.L. carried out the XPS analysis. S.K. performed the TEM analysis. J.-M.L. and K.-Y.P. conducted the electrochemical measurements. All authors contributed to writing and revising the manuscript.

DECLARATION OF INTERESTS

The authors declare no competing interests.

Received: June 4, 2020
Revised: July 3, 2020
Accepted: July 9, 2020
Published: August 5, 2020

REFERENCES

1. Tarascon, J.M., and Armand, M. (2001). Issues and challenges facing rechargeable lithium batteries. Nature *414*, 359–367.
2. Goodenough, J.B., and Park, K.S. (2013). The Li-ion rechargeable battery: a perspective. J. Am. Chem. Soc. *135*, 1167–1176.
3. Lu, L.G., Han, X.B., Li, J.Q., Hua, J.F., and Ouyang, M.G. (2013). A review on the key issues for lithium-ion battery management in electric vehicles. J. Power Sources *226*, 272–288.
4. Son, I.H., Park, J.H., Park, S., Park, K., Han, S., Shin, J., Doo, S.G., Hwang, Y., Chang, H., and Choi, J.W. (2017). Graphene balls for lithium rechargeable batteries with fast charging and high volumetric energy densities. Nat. Commun. *8*, 1561.
5. Dahn, J.R., Zheng, T., Liu, Y.H., and Xue, J.S. (1995). Mechanisms for lithium insertion in carbonaceous materials. Science *270*, 590–593.
6. Ming, J., Cao, Z., Wahyudi, W., Li, M.L., Kumar, P., Wu, Y.Q., Hwang, J.Y., Hedhili, M.N., Cavallo, L., Sun, Y.K., et al. (2018). New insights on graphite anode stability in rechargeable batteries: Li ion coordination structures prevail over solid electrolyte interphases. ACS Energy Lett. *3*, 335–340.
7. Scrosati, B., and Garche, J. (2010). Lithium batteries: status, prospects and future. J. Power Sources *195*, 2419–2430.
8. Goriparti, S., Miele, E., De Angelis, F., Di Fabrizio, E., Zaccaria, R.P., and Capiglia, C. (2014). Review on recent progress of nanostructured anode materials for Li-ion batteries. J. Power Sources *257*, 421–443.
9. Nitta, N., Wu, F.X., Lee, J.T., and Yushin, G. (2015). Li-ion battery materials: present and future. Mater. Today *18*, 252–264.
10. Li, W.Y., Yao, H.B., Yan, K., Zheng, G.Y., Liang, Z., Chiang, Y.M., and Cui, Y. (2015). The synergetic effect of lithium polysulfide and lithium nitrate to prevent lithium dendrite growth. Nat. Commun. *6*, 7436.
11. Boukamp, B.A., Lesh, G.C., and Huggins, R.A. (1981). All-solid lithium electrodes with mixed-conductor matrix. J. Electrochem. Soc. *128*, 725–729.
12. Chan, C.K., Peng, H.L., Liu, G., McIlwrath, K., Zhang, X.F., Huggins, R.A., and Cui, Y. (2008). High-performance lithium battery anodes using silicon nanowires. Nat. Nanotechnol. *3*, 31–35.
13. Zaghib, K., Simoneau, M., Armand, M., and Gauthier, M. (1999). Electrochemical study of $Li_4Ti_5O_{12}$ as negative electrode for Li-ion polymer rechargeable batteries. J. Power Sources *81*, 300–305.
14. Aldon, L., Kubiak, P., Womes, M., Jumas, J.C., Olivier-Fourcade, J., Tirado, J.L., Corredor, J.I., and Vicente, C.P. (2004). Chemical and electrochemical Li-insertion into the $Li_4Ti_5O_{12}$ spinel. Chem. Mater. *16*, 5721–5725.
15. Yi, T.F., Jiang, L.J., Shu, J., Yue, C.B., Zhu, R.S., and Qiao, H.B. (2010). Recent development and application of $Li_4Ti_5O_{12}$ as anode material of lithium ion battery. J. Phys. Chem. Solids *71*, 1236–1242.
16. Griffith, K.J., Forse, A.C., Griffin, J.M., and Grey, C.P. (2016). High-rate intercalation without nanostructuring in metastable Nb_2O_5 bronze phases. J. Am. Chem. Soc. *138*, 8888–8899.

17. Griffith, K.J., Wiaderek, K.M., Cibin, G., Marbella, L.E., and Grey, C.P. (2018). Niobium tungsten oxides for high-rate lithium-ion energy storage. Nature *559*, 556–563.

18. Sun, H.T., Mei, L., Liang, J.F., Zhao, Z.P., Lee, C., Fei, H.L., Ding, M.N., Lau, J., Li, M.F., Wang, C., et al. (2017). Three-dimensional holey-graphene/niobia composite architectures for ultrahigh-rate energy storage. Science *356*, 599–604.

19. Liu, J.Y., Pang, W.K., Zhou, T., Chen, L., Wang, Y.G., Peterson, V.K., Yang, Z.Q., Guo, Z.P., and Xia, Y.Y. (2017). Li_2TiSiO_5: a low potential and large capacity Ti-based anode material for Li-ion batteries. Energy Environ. Sci. *10*, 1456–1464.

20. Liu, J.Y., Liu, Y., Hou, M.Y., Wang, Y.G., Wang, C.X., and Xia, Y.Y. (2018). Li_2TiSiO_5 and expanded graphite nanocomposite anode material with improved rate performance for lithium-ion batteries. Electrochim. Acta *260*, 695–702.

21. Wang, S.J., Wang, R.T., Bian, Y., Jin, D.D., Zhang, Y.B., and Zhang, L. (2019). In-situ encapsulation of pseudocapacitive Li_2TiSiO_5 nanoparticles into fibrous carbon framework for ultrafast and stable lithium storage. Nano Energy *55*, 173–181.

22. Liu, N., Lu, Z.D., Zhao, J., McDowell, M.T., Lee, H.W., Zhao, W.T., and Cui, Y. (2014). A pomegranate-inspired nanoscale design for large-volume-change lithium battery anodes. Nat. Nanotechnol. *9*, 187–192.

23. Chen, K.S., Xu, R., Luu, N.S., Secor, E.B., Hamamoto, K., Li, Q.Q., Kim, S., Sangwan, V.K., Balla, I., Guiney, L.M., et al. (2017). Comprehensive enhancement of nanostructured lithium-ion battery cathode materials via conformal graphene dispersion. Nano Lett. *17*, 2539–2546.

24. Jaber-Ansari, L., Puntambekar, K.P., Kim, S., Aykol, M., Luo, L.L., Wu, J.S., Myers, B.D., Iddir, H., Russell, J.T., Saldana, S.J., et al. (2015). Suppressing manganese dissolution from lithium manganese oxide spinel cathodes with single-layer graphene. Adv. Energy Mater. *5*, 1500646.

25. Wang, C., Wang, S.A., He, Y.B., Tang, L.K., Han, C.P., Yang, C., Wagemaker, M., Li, B.H., Yang, Q.H., Kim, J.K., et al. (2015). Combining fast Li-ion battery cycling with large volumetric energy density: grain boundary induced high electronic and ionic conductivity in $Li_4Ti_5O_{12}$ spheres of densely packed nanocrystallites. Chem. Mater. *27*, 5647–5656.

26. Singh, D.P., Mulder, F.M., and Wagemaker, M. (2013). Templated spinel $Li_4Ti_5O_{12}$ Li-ion battery electrodes combining high rates with high energy density. Electrochem. Commun. *35*, 124–127.

27. Billaud, J., Bouville, F., Magrini, T., Villevieille, C., and Studart, A.R. (2016). Magnetically aligned graphite electrodes for high-rate performance Li-ion batteries. Nat. Energy *1*, 16097.

28. Secor, E.B., Prabhumirashi, P.L., Puntambekar, K., Geier, M.L., and Hersam, M.C. (2013). Inkjet printing of high conductivity, flexible graphene patterns. J. Phys. Chem. Lett. *4*, 1347–1351.